

Article

# Enhanced Formability and Accelerated Precipitation Behavior of 7075 Al Alloy Extruded Rod by High Temperature Aging

Ming-Hsiang Ku , Fei-Yi Hung \* , Truan-Sheng Lui and Jyun-Jhih Lai

Department of Materials Science and Engineering, National Cheng Kung University, Tainan 701, Taiwan; lenno6622@gmail.com (M.-H.K.); luits@mail.ncku.edu.tw (T.-S.L.); defendor@outlook.com (J.-J.L.)

\* Correspondence: fyhung@mail.ncku.edu.tw; Tel./Fax: +6-275-7575 (ext. 62950)

Received: 30 July 2018; Accepted: 13 August 2018; Published: 17 August 2018



**Abstract:** This study was conducted for high temperature aging (HTA) to simultaneously reduce current treatment time and increase the tensile ductility of 7075 aluminum alloy. Various high temperatures and different durations for artificial aging were compared. We investigated the microstructure and the tensile properties of 7075 aluminum alloy extruded rod after various HTAs, and compared them with the outcomes of full annealing (O). The total elongation (TE) of the specimen after solution heat treatment (490 °C, 1 h) and artificial aging (280 °C, 12 h) was about 25%. For full annealing, it is known as 21%. The reason for this was the formation of the  $\eta$  phase in the matrix, which had fewer large particles (Al-Cu phase). The hardening of HTA specimens is higher than that of O, indicating necking resistance during homogeneous plastic deformation. Thereby, HTA treatment increases the formability of 7075 aluminum alloy.

**Keywords:** 7075 aluminum alloy; high temperature aging (HTA); tensile ductility; formability

## 1. Introduction

The 7075 aluminum alloy is a kind of precipitation-hardened aluminum alloy, with high specific strength, and high fracture toughness. It is widely used for lightweight and high-strength structural parts, such as aircraft wings, pipe fittings, and automobiles [1–3]. The precipitation hardening mechanism of 7075 aluminum alloy employs two strengthening phases, Guinier-Preston zones (GP-zones), and an  $\eta'$  phase, depicted by the precipitation sequence [4,5]: Supersaturated solid solution  $\rightarrow$  GP-zones (spherical)  $\rightarrow$   $\eta'$   $\rightarrow$   $\eta$ .

Here, the GP-zones are fully coherent with the Al matrix and the interface energy is low. The main hardening precipitate,  $\eta'$ , is a metastable hexagonal phase, semi-coherent with the Al matrix ( $a = 0.496 \text{ nm} \cong [211]_{2\text{Al}}$ ;  $c = 1.40 \text{ nm} \cong 2[111]_{\text{Al}}$ , where  $a_{\text{Al}} = 0.405 \text{ nm}$ ) [6,7]. The equilibrium phase,  $\eta$ , is a hexagonal laves phase, with  $a = 0.5221 \text{ nm}$ ,  $c = 0.8567 \text{ nm}$  [8,9].

According to the industrial applications, the aging temperature ranges from 100 °C to 170 °C. The T6 temper is produced by a peak aging treatment at 120 °C. The aging treatment for the T73 temper has the first aging step at low temperature (100 °C) followed by a second treatment at a higher temperature (160–170 °C). Typically, the T73 temper is commonly one of post-process heat treatment (PPHT) for 7075 aluminum alloy [10,11]. After PPHT, the notch sensitivity and the stress corrosion resistance of the alloy are improved [12,13]. Bending and forging can easily make the 7075 aluminum alloy crack. The bending position is used for making bumpers and other structural parts.

A large number of current papers address PPHT aiming at improving tensile ductility. Full annealing is such a heat treatment, widely used for increasing ductility and decreasing plastic deformation resistance. The full annealing of 7075 aluminum alloy is a two-step heat treatment [14,15],

which is both time and energy consuming. Ertürk et al. [16] indicated that aging at 120 °C for 150 h improves tensile ductility and workability of 7075 aluminum alloy more than natural aging and peak aging. Thus, our goal was to develop a heat treatment with reduced time and increased tensile ductility and formability. The tensile ductility of Al-Zn-Mg aluminum alloy and 2024 aluminum alloy was greatly increased via solution treatment and water quenching (W heat treatment) [17,18]. The main reason is that the solutes are completely dissolved in the matrix. The sample after W heat treatment has a high initial elongation, but it processes natural aging behavior (mechanical properties increasing) and causing lower workability.

The precipitation hardening mechanism for 7075 aluminum alloy mainly depends on the interaction among the GP-zones, a part of the  $\eta'$  phase, and the dislocation in the matrix. As the aging temperature and time increase, the  $\eta$  phase replaces the GP-zones and the  $\eta'$  phase. The precipitation strengthening effect results in the deterioration of strength, that is, in improved ductility [19,20].

The goal of the present study is to evaluate the effects of varying temperature and aging time during high temperature aging (HTA) (non-traditional and rapid) on the microstructure and tensile properties of 7075 aluminum alloy. We chose full annealing as the reference treatment for comparison. To meet the requirements of plastic processing, we need: (1) improved formability and (2) tensile ductility of 25% or higher.

## 2. Experiment Procedure

Table 1 shows the chemical composition of the 7075 aluminum alloy extruded rod used. The reference treatment was full annealing (O), and the other one was high temperature aging (HTA). The four HTA group names (HTA240-8, HTA280-6, HTA280-12, and HTA280-18) symbolize the four sets of conditions used. The aging temperature was chosen by differential scanning calorimetry (DSC) (Figure 1) [21] and by the aging hardness curve (Figure 2). The hardness results of HTA treatment at 280 °C were similar to those of full annealing. Table 2 shows the treatment procedures.

**Table 1.** Chemical composition of the 7075 aluminum alloy extruded rod (mass %).

Zn	Mg	Cu	Cr	Fe	Si	Al
5.80	2.53	1.64	0.23	0.09	0.05	Bal.

**Table 2.** Experimental conditions and specimen codes.

Symbol	Procedure
HTA240-8	Heating at 490 °C for 1 h then quenching, and heating at 240 °C for 8 h and air cooling.
HTA280-6	Heating at 490 °C for 1 h then quenching, and heating at 280 °C for 6 h and air cooling.
HTA280-12	Heating at 490 °C for 1 h then quenching, and heating at 280 °C for 12 h and air cooling.
HTA280-18	Heating at 490 °C for 1 h then quenching, and heating at 280 °C for 18 h and air cooling.
O	Heating at 415 °C for 2 h then furnace cooling at 20 °C/h cooling rate to 230 °C, holding for 6 h and furnace cooling.

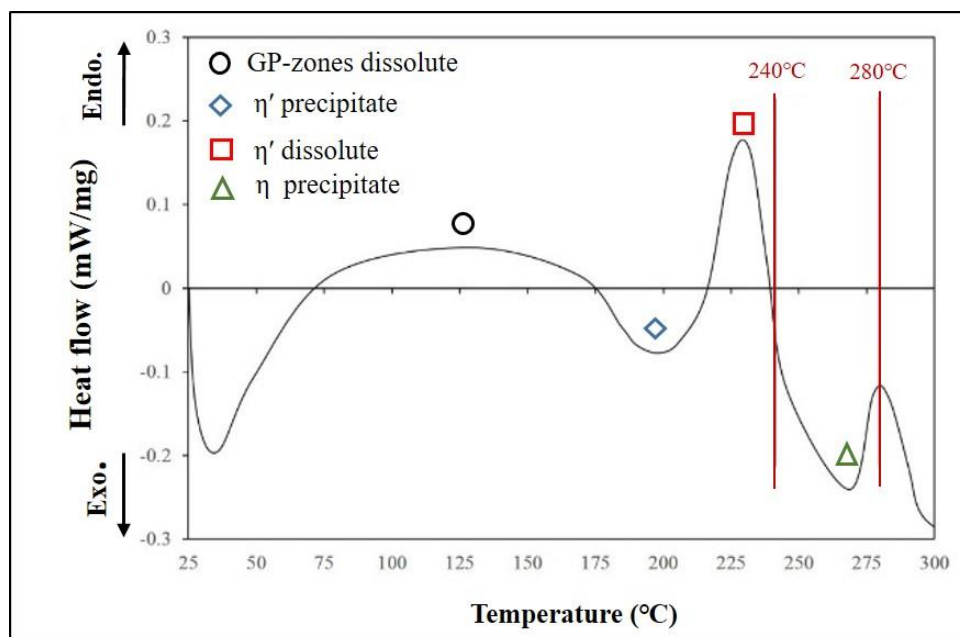


Figure 1. Differential scanning calorimetry (DSC) analysis of the 7075 aluminum alloy extruded rod.

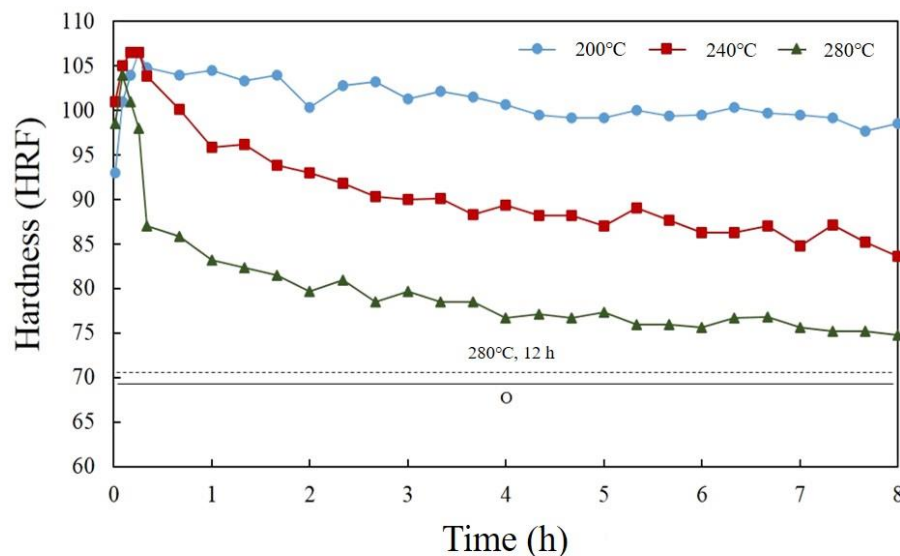


Figure 2. The aging hardness curves of the 7075 aluminum alloy extruded rod during different treatments.

The microstructure and the distribution of the second particle phase were examined by optical microscope (OM, OLYMPUS BX41M-LED, OLYMPUS, Tokyo, Japan). The chemical compositions of the second phase and the fracture surfaces were evaluated by a scanning electron microscope (SEM, HITACHI SU-5000, HITACHI, Tokyo, Japan) equipped with an energy dispersive spectrometer (EDS).

X-ray diffraction (XRD, Bruker AXS GmbH, Karlsruhe, Germany) analysis with Cu K $\alpha$  ( $\lambda = 1.541838 \text{ \AA}$ ) radiation was employed for  $20^\circ \leq 2\theta \leq 90^\circ$  to identify the phase transformation of 7075 aluminum alloy after HTA and O.

The microstructure and the chemical composition of the precipitate were analyzed by transmission electron microscope (TEM, Tecnai F20 G2, EFI, Hillsboro, OR, USA). The TEM specimens were mechanically thinned down to 100  $\mu\text{m}$  in thickness. Disk of 3-mm diameter was subsequently thinned by twin-jet electro-polishing, using a solution of 20% HClO $_4$  and 80% ethanol at  $-25^\circ\text{C}$ . TEM was

performed by an FEI EO Tecnai F20 G2 Field-Emission TEM (Tecnai F20 G2, EFI, Hillsboro, OR, USA), operating at 120 KV.

Tensile tests were conducted at room temperature to clarify the effects of tensile force during working processes like bending and forging. The axis of the tensile specimen was parallel to the extrusion direction. The dimensions of the tensile specimen are shown in Figure 3. The tensile test was performed with a universal testing machine (HT-8336, Hung Ta, Taichung, Taiwan) at an initial strain rate of  $1.7 \times 10^{-3} \text{ s}^{-1}$ .

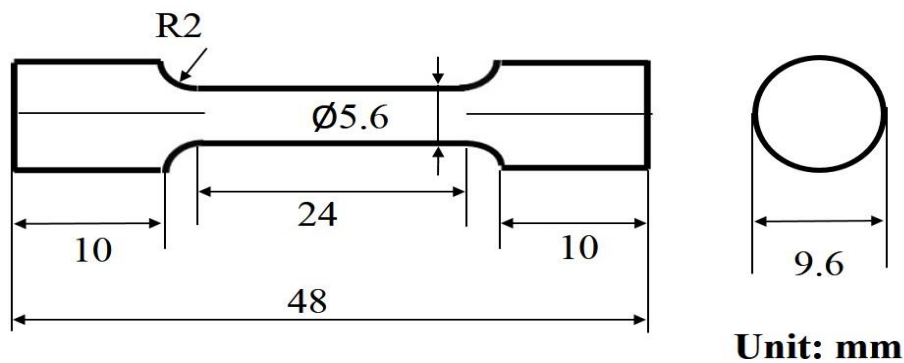


Figure 3. Schematic illustration of the tensile rod specimen.

### 3. Results and Discussion

#### 3.1. The Microstructure of 7075 Aluminum Alloy Extruded Rod after Various Post-Process Heat Treatments (PPHTs)

Figure 4 shows the microstructure of 7075 Al alloy after O. Figure 4a shows the morphology of the O specimen with average grain size of  $62 \mu\text{m}$ . There are many second phase particles in the matrix, as shown in Figure 4b. The morphology and the composition of second phase particles come from the SEM/EDS (Figure 4c,d, and Table 3) and XRD data (Figure 5). The second phase particles can be divided into two types: (1) Al-Cu composition, including  $\text{Al}_2\text{CuMg}$  phase (lath-like or irregular) with particle size from  $1 \mu\text{m}$  to  $5 \mu\text{m}$  and (2) Al-Zn-Mg-Cu phase (irregular) with particle size from  $3 \mu\text{m}$  to  $10 \mu\text{m}$ . In addition, the smaller particles ( $<1 \mu\text{m}$ ) are  $\eta$  phase ( $\text{MgZn}_2$ ) as determined by our XRD analysis and the reports [22,23].

According to reports [15] and our own verification, the second phase particles and  $\text{MgZn}_2$  in the matrix became coarse during two-step full annealing. The alloy in the matrix became much softer, yielding higher ductility and improved formability.

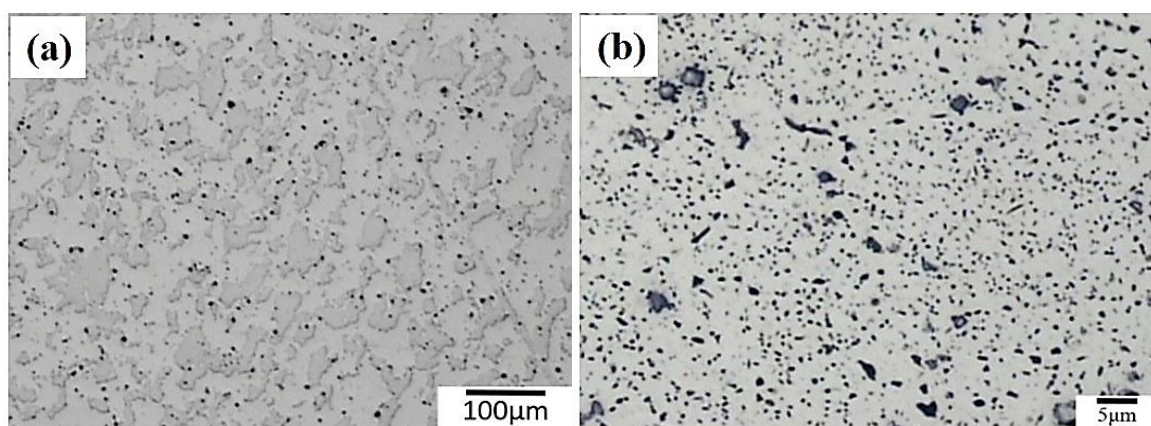
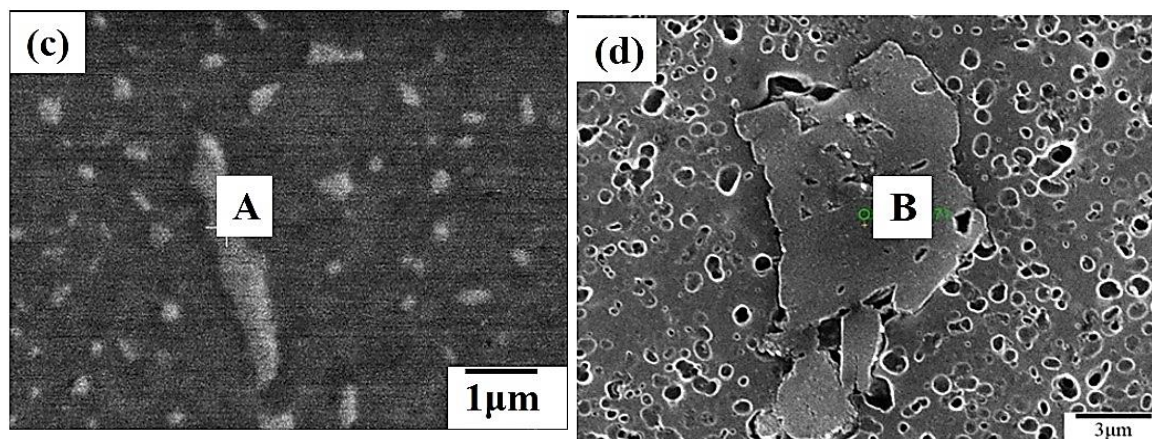


Figure 4. Cont.

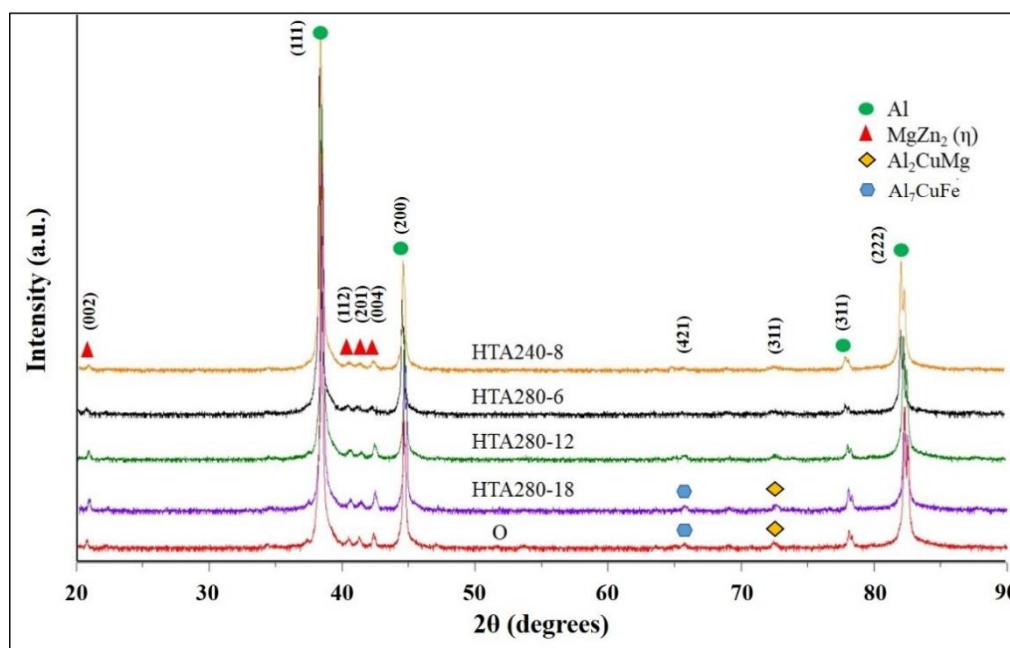


**Figure 4.** The morphology and the distribution of second phase particles for O specimen: (a,b) display various magnifications; (c,d) display various second phase particles in the matrix.

**Table 3.** Energy dispersive spectrometer (EDS) data for specimens shown in Figure 4c,d.

	Al	Zn	Mg	Cu
A	59.4	0.6	21.0	19.0
B	81.2	0.7	1.4	16.7

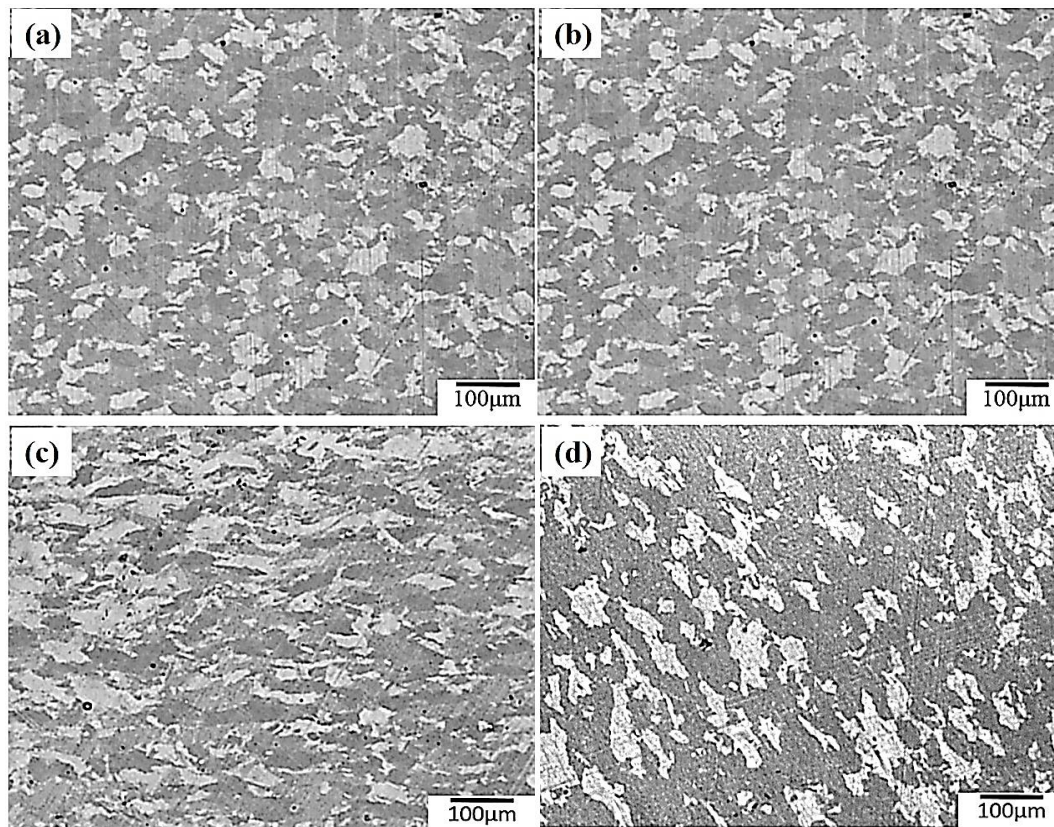
Unit: at. %.



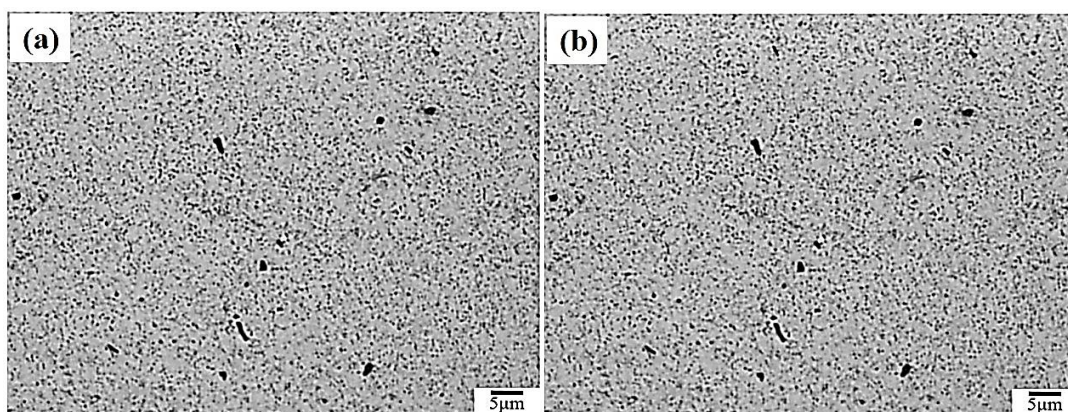
**Figure 5.** XRD analysis of 7075 Al alloy extruded rod after various PPHTs.

Figure 6 shows the microstructures after various high temperature aging treatments. The morphology of the four HTA specimens was similar, with average grain sizes between 52  $\mu\text{m}$  and 56  $\mu\text{m}$ . From the SEM/EDS data, we found that the second phase particles of HTA specimens mainly included an  $\text{Al}_2\text{Cu}$  phase and an Al-Zn-Mg-Cu phase, as shown in Figure 7 and Table 4. In addition, there were many other finer particles ( $<1 \mu\text{m}$ ) in the matrix. Based on the literature [24,25] and our XRD data (Figure 5) along with TEM analysis (Figure 8), the finer particles are an  $\eta$  phase with hexagonal close-packed (HCP) structure and particles sizes from 100 nm to 150 nm.

We infer that different heat treatments resulted in different microstructures for the O specimen and the HTA specimens. The O specimen had an  $\eta$  phase and many larger particles, mainly  $Al_2CuMg$  phase and Al-Zn-Mg-Cu phase. In the matrix of the HTA specimens, we found a high-density distribution  $\eta$  phase, an  $\eta'$  phase, and a small amount of Al-Cu phase. The amount of the  $\eta$  phase and the  $\eta'$  phase varied by the aging temperature.



**Figure 6.** Microstructure of 7075 Al alloy extruded rod after various high temperature artificial aging treatments: (a) HTA240-8; (b) HTA280-6; (c) HTA280-12; (d) HTA280-18.



**Figure 7.** Cont.

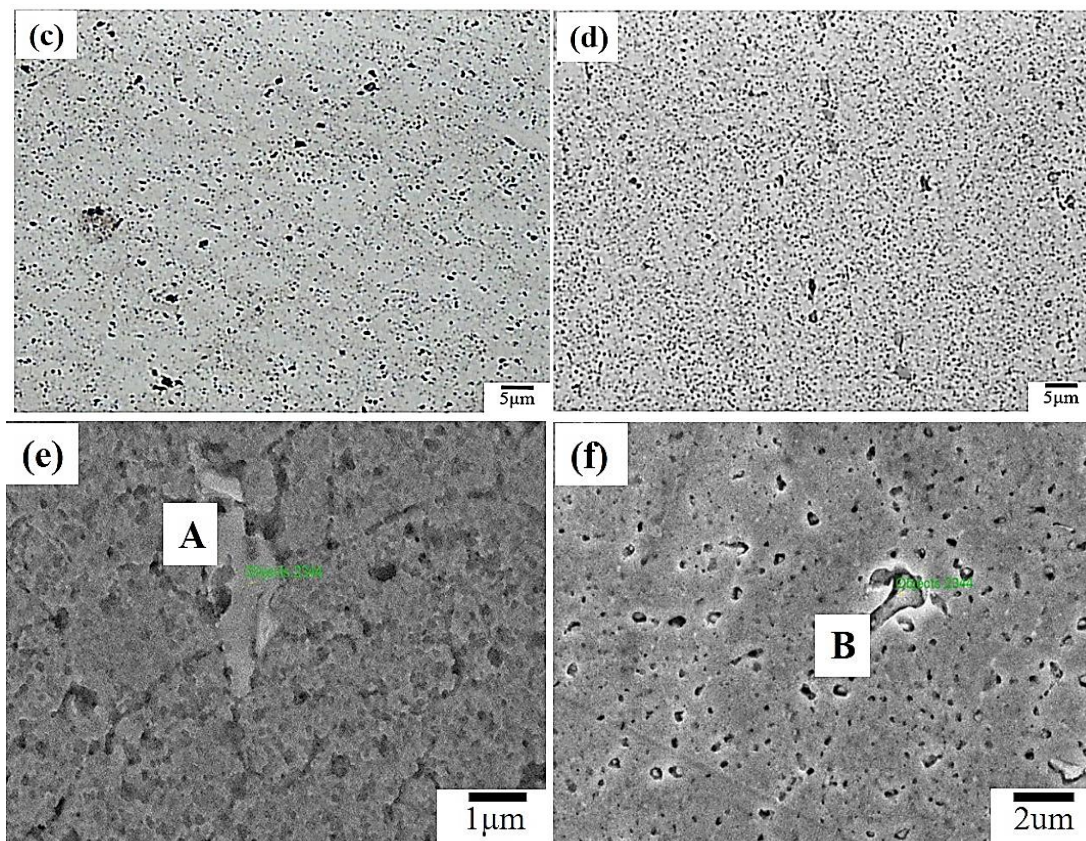


**Figure 7.** The morphology and the distribution of second phase particles for various HTA specimens: (a) HTA240-8; (b) HTA280-6; (c) HTA280-12; (d) HTA280-18; (e) HTA240-8 (high magnification); (f) HTA280-18 (high magnification).

**Table 4.** EDS data for specimens shown in Figure 7e,f.

	Al	Zn	Mg	Cu
A	87.7	0	1.1	11.2
B	60.0	5.06	2.71	31.32

Unit: at. %.

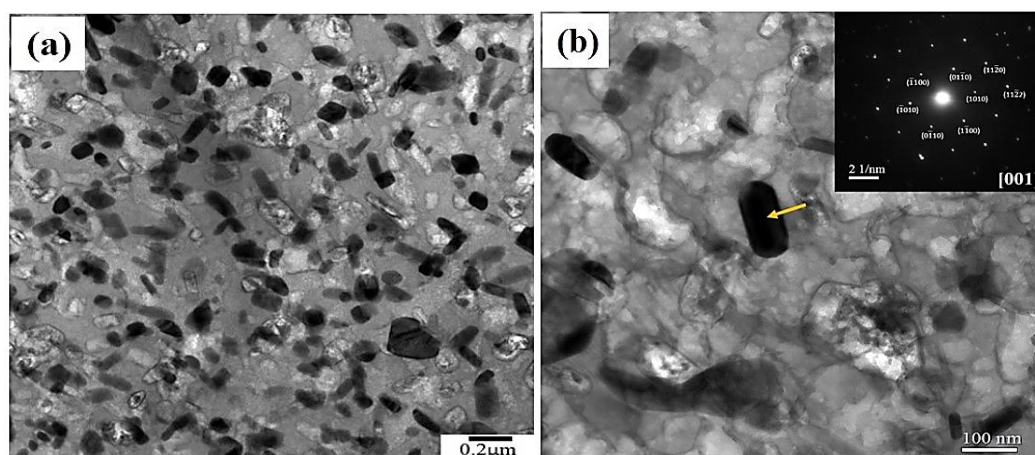


**Figure 8.** TEM micrographs and selected area diffraction patterns (SADP) of HTA280-12 specimen: (a) matrix; (b)  $[001]_{Al}$  SADP.

### 3.2. Tensile Properties of 7075 Aluminum Alloy Extruded Rod after Various PPHTs at Room Temperature

The deformation behavior of the plastic region at various PPHTs was determined by tensile test [26–29]. Figure 9 reveals the stress-strain flow curve of the specimens after various PPHTs at room temperature. These results indicate dynamic strain aging (DSA) in view of the tensile deformation flow curves of all PPHT tensile specimens. Based on the literature [30,31], this phenomenon is a type A serrated flow.

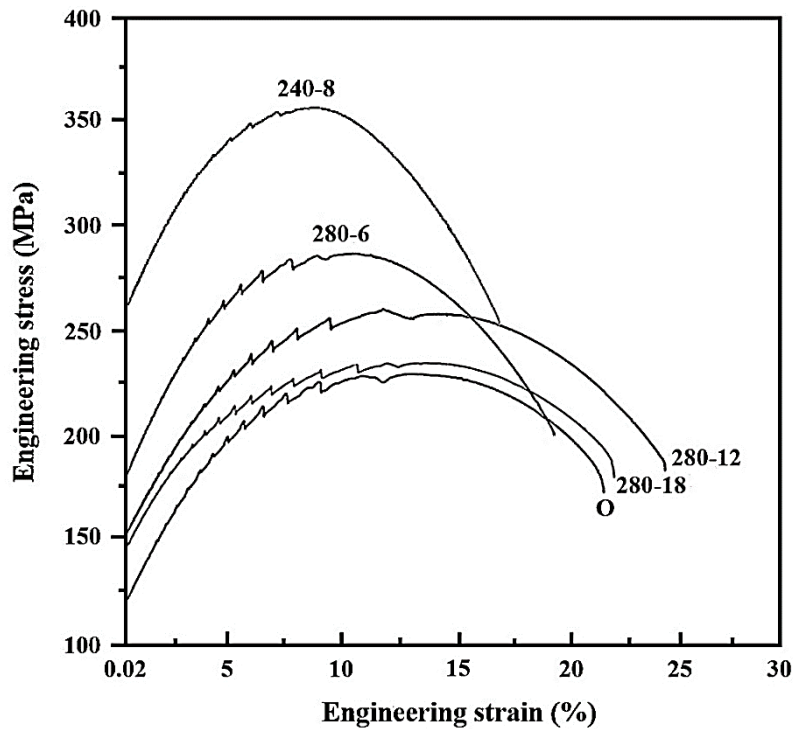
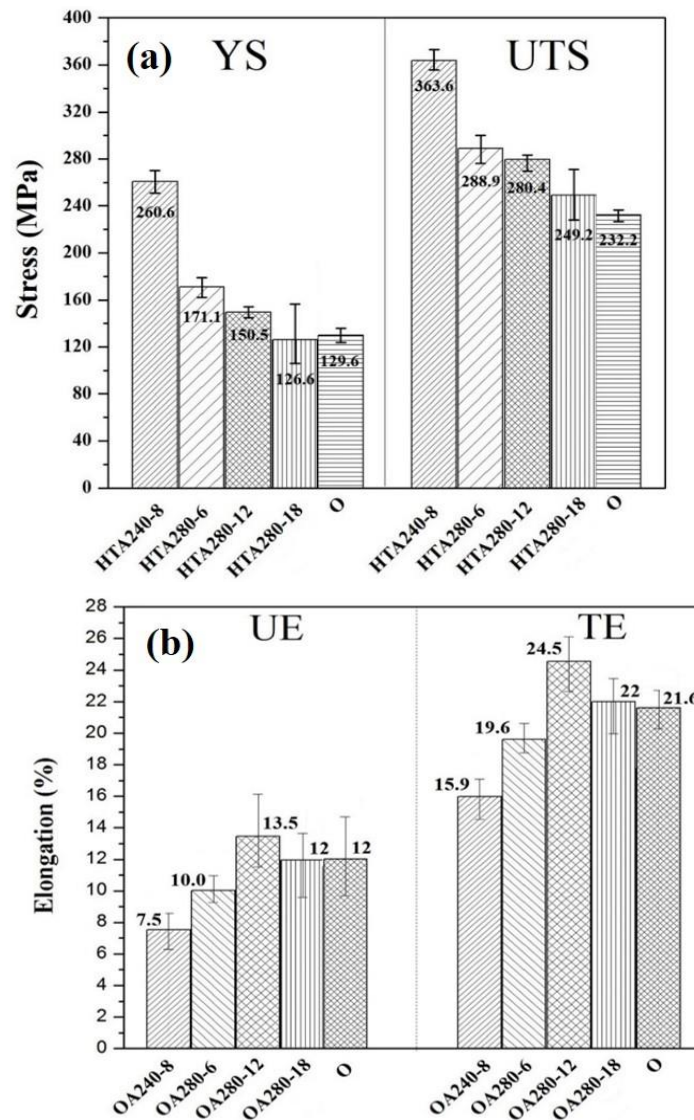


Figure 9. Stress-strain flow curve of 7075 Al alloy extruded rod after various PPHTs.

The yield strength (YS) and the ultimate tensile strength (UTS) of the HTA240-8 specimen are the highest, while those of the O specimen are the lowest, as seen in Figure 10a. The tensile strength of the HTA specimens deteriorated by aging temperature between 240 °C and 280 °C. By increasing the extent of aging, uniform elongation (UE) and total elongation (TE) also increased. Among all PPHT specimens, HTA280-12 had the best performance (about 25% in TE), and HTA240-8 had the lowest ductility, as shown in Figure 10b.

We wonder, what factors affected the ductility of the HTA280-18 specimen. From DSC analysis (Figure 1) and the literature [22,32], at 240 °C, the endothermic reaction of HTA240-8 is actually the dissolution of the  $\eta'$  phase due to the highest strength. At 280 °C, the  $\eta$  phase was formed during the peak of the exothermic reaction, and it replaced the  $\eta'$  phase. Hence, the highest ductility was found in HTA280-12 because a significant  $\eta$  phase was formed in the matrix. At aging temperatures beyond 280 °C, the dissolution of  $\eta$  becomes endothermic, inducing natural aging and lower ductility.



**Figure 10.** Tensile properties of 7075 Al alloy extruded rod after various PPHTs: (a) strength; (b) elongation.

### 3.3. The Tensile Fracture and the Working Hardness of PPHT Specimens

Figure 11 reveals the morphology of the fracture surface of tensile specimens. All tensile specimens have obvious necking near the fracture plane. The fracture plane presents cup- and cone-type ductile fractures.

Figure 12 shows the fracture surface of tensile specimens, including HTA 280-12, HTA240-8, and O. There are many dimples on the fracture surface. The large second phase particles and the precipitates are located near the dimples. From the previous study [33], the nucleation of microvoid and microcrack located frequently at around the second phase particles. These defects form cracks if they are induced by larger particles. From Figures 4 and 6, the O specimen has more large-size phase particles than the HTA group has in the matrix. Hence, the O specimen could connect large microvoids and microcracks into fractures. Thus, the O specimen has lower TE than HTA280-12, even if HTA280-12 has higher strength.

In order to evaluate necking resistance during homogeneous plastic deformation [23], the work hardening rate of all PPHT specimens was analyzed, see Figure 13. The work hardening curves of all PPHT specimens during homogeneous plastic deformation decreases by plastic strain. HT240-8 has

the highest rate at the beginning of a homogeneous plastic deformation, then it drops off immediately. The work hardening rate of HTA specimens is higher than that of O, indicating higher necking resistance. Thereby, HTA treatment increases the formability of the plate material and it will not fracture easily during tensile deformation like forging and deep drawing [34].



**Figure 11.** Macrostructures of tensile fracture of 7075 Al alloy extruded rod with various PPHTs: (a) specimens after tensile test; (b) the fracture surfaces.

A schematic diagram in Figure 14 displays the relationships among formability, elongation, and microstructure. The formability of 7075 aluminum alloy increases with aging temperature and with aging time up to 280 °C for 12 h. The main reason is that the precipitates change from the GP-zones and the  $\eta'$  phase to a lesser  $\eta'$  phase and a greater  $\eta$  phase. The precipitation strength decreases, and the ductility increases. In addition, the HTA specimens have fewer large particles in the matrix than the O does.

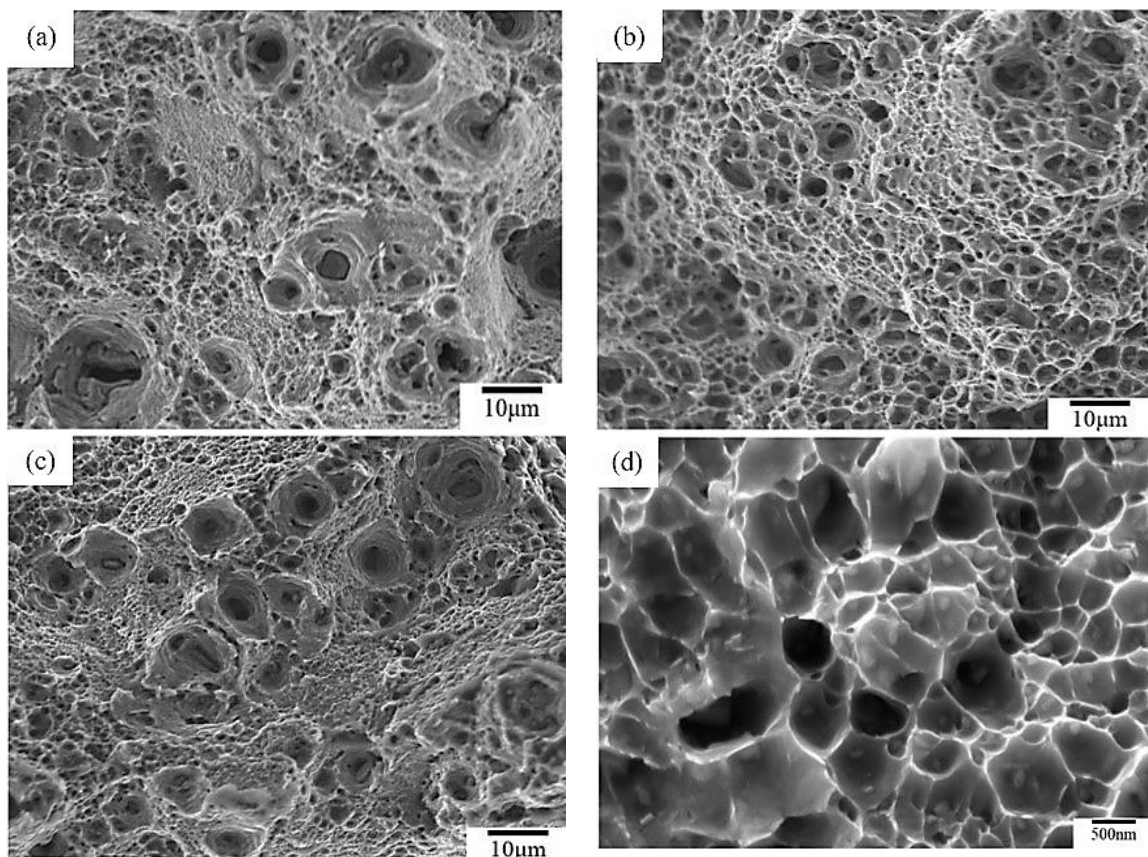


**Figure 12.** Fracture surfaces of 7075 Al alloy extruded rod with various PPHTs: (a) HTA240-8; (b) HTA280-12; (c) O; (d) HTA280-12 (high magnification).

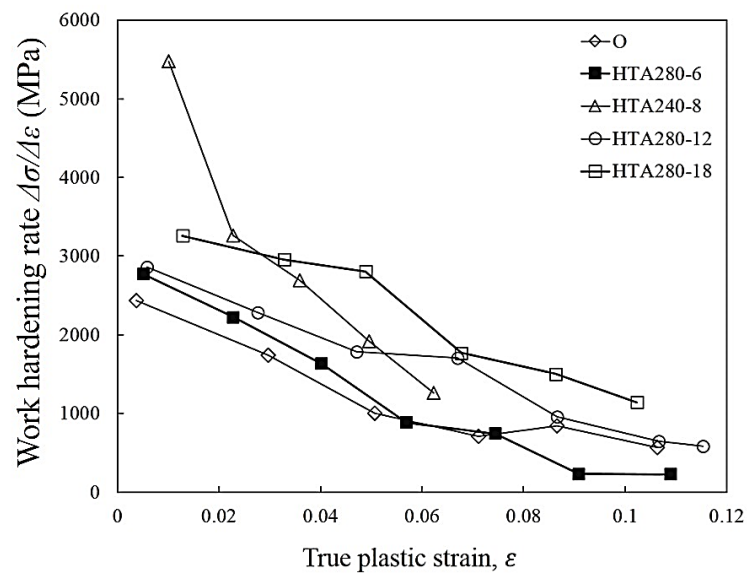


**Figure 13.** Work hardening curves of 7075 Al alloy extruded rod with various PPHTs.

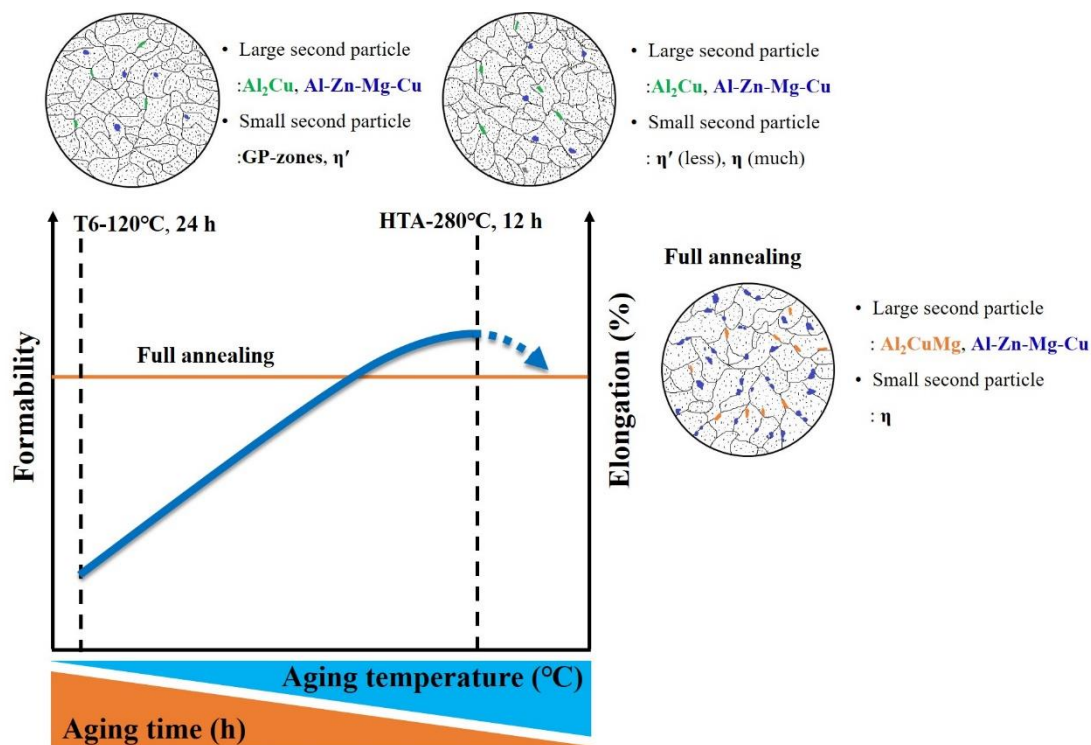


**Figure 14.** A schematic diagram of the relationships among formability, elongation, and microstructure for 7075 aluminum alloy after various PPHTs.

#### 4. Conclusions

The microstructure and tensile properties of 7075 aluminum alloy extruded rod via various high temperature aging and full annealing treatments were investigated and compared:

1. High temperature aging can decrease precipitate hardening by the formation of an η phase.
2. The high temperature aging at 280 °C, 12 h had fewer large particles (Al-Cu phase) in the Al matrix than full annealing did. The nucleation of microvoid and microcrack was located frequently around the large particles. The defects form cracks mainly and cause the fractures of the sample. Hence, the high temperature aging at 280 °C, 12 h presented to be superior over full annealing in regard to the work hardening rate and formability.
3. High temperature aging can increase ductility only in a temperature range. At aging temperatures beyond 280 °C, the dissolution of η becomes endothermic, inducing natural aging and lower ductility.

**Author Contributions:** M.-H.K. analyzed the data, and wrote the paper. F.-Y.H. and T.-S.L. are advisers. J.-J.L. performed the experiments, and analyzed the data.

**Funding:** The authors are grateful to The Instrument Center of National Cheng Kung University and the Ministry of Science and Technology of Taiwan (Grant No. MOST 106-2221-E-006-064) for their financial support for this research.

**Conflicts of Interest:** The authors declare no conflicts of interest.

#### References

1. De Sanctis, M. Structure and properties of rapidly solidified ultrahigh strength Al–Zn–Mg–Cu alloys produced by spray deposition. *Mater. Sci. Eng. A* **1991**, *141*, 103–121. [[CrossRef](#)]
2. Starke, E.A., Jr.; Staley, J.T. Application of modern aluminum alloys to aircraft. *Prog. Aerospace Sci.* **1996**, *32*, 131–172. [[CrossRef](#)]

3. Liu, J. Advanced Aluminum and Hybrid Aerostructures for Future Aircraft. *Mater. Sci. Forum.* **2006**, 519–521, 1233–1238. [[CrossRef](#)]
4. Mondolfo, L.F.; Gjostein, N.A.; Levinson, D.W. Structural Changes during the Aging in an Al-Mg-Zn Alloy. *JOM* **1956**, *10*, 1378–1385. [[CrossRef](#)]
5. Hatch, J.E. *Aluminum: Properties and Physical Metallurgy*, 1st ed.; American Society for Metals: Geauga County, OH, USA, 1984; pp. 145–158, ISBN 0-87170-176-6.
6. Gjønnes, J.; Simensen, C. An Electron Microscope Investigation of the Microstructure in an Aluminium-Zinc-Magnesium Alloy. *Acta Metall.* **1970**, *18*, 881–890. [[CrossRef](#)]
7. Degischer, H.P.; Lacom, W.; Zahra, A.M.; Zahra, C.Y. Decomposition Processes in an Al-5% Zn-1% Mg Alloy. II.—Electronmicroscopic Investigations. *Z. Metallk.* **1980**, *71*, 231–238.
8. Friauf, J.B. The Crystal Structure of Magnesium Di-Zincide. *Phys. Rev.* **1927**, *29*, 34–40. [[CrossRef](#)]
9. Komura, Y.; Tokunaga, K. Structural Studies of Stacking Variants in Mg-base Friauf-Laves phases. *Acta Cryst.* **1980**, *B36*, 1548–1554. [[CrossRef](#)]
10. Dorward, R.C.; Hasse, K.R. *Flaw Growth of 7075, 7475, 7050 and 7049 Aluminum Plate in Stress Corrosion Environments*; Research Final Report: Contact No. NAS8-30890; Kaiser Aluminum & Chemical Corporation: Foothill Ranch, CA, USA, 1976.
11. Oñoro, J. The stress corrosion cracking behaviour of heat-treated Al-Zn-Mg-Cu alloy in modified salt spray fog testing. *Mater. Corros.* **2010**, *61*, 125–129.
12. Gruhl, W. Stress Corrosion Cracking of High Strength Aluminum Alloys. *Z. Metallkd.* **1984**, *75*, 819–826.
13. Park, J.K. Influence of Retrogression and Reaging Treatments on the Strength and Stress Corrosion Resistance of Aluminium alloy 7075-T6. *Mater. Sci. Eng. A* **1988**, *103*, 223–231. [[CrossRef](#)]
14. Sessler, J.; Welss, V. *Metallurgy. Materials Data Handbook: Aluminum Alloy 7075*, 1st ed.; National Aeronautics and Space Administration: Huntsville, AL, USA, 1967; Chapter 3, pp. 9–23.
15. Hatch, J.E. *Aluminum: Properties and Physical Metallurgy*, 1st ed.; American Society for Metals: Geauga County, OH, USA, 1984; pp. 152–153, ISBN 0-87170-176-6.
16. Ertürk, T.; Kazazoglu, E. Effect of aging on bulk formability of aluminum alloys. In *Formability of Metallic materials—2000*, 1st ed.; Newby, J.R., Niemeier, B.A., Eds.; American Society for Testing and Materials: Chicago, IL, USA, 1982; pp. 19–34.
17. Deschamps, A.; Niewczas, M.; Bley, F.; Brechet, Y.; Embury, J.D.; Le Sinq, L.; Livet, F.; Simon, J.P. Low-temperature dynamic precipitation in a supersaturated Al-Zn-Mg alloy and related strain hardening. *Philos. Mag.* **1999**, *79*, 2485–2504. [[CrossRef](#)]
18. Kim, W.J.; Chung, C.S.; Ma, D.S.; Hong, S.I.; Kim, H.K. Optimization of strength and ductility of 2024 Al by equal channel angular pressing (ECAP) and post-ECAP aging. *Scr. Mater.* **2003**, *49*, 333–338. [[CrossRef](#)]
19. Rajan, K.; Wallace, W.; Beddoes, J.C. Microstructural study of a high-strength stress-corrosion resistant 7075 aluminium alloy. *J. Mater. Sci.* **1982**, *17*, 2817–2824. [[CrossRef](#)]
20. Staley, J.T. Aging kinetics of aluminum alloy 7050. *Metall. Mater. Trans. B* **1974**, *5*, 929–932. [[CrossRef](#)]
21. Chen, Z.; Mo, Y.; Nie, Z. Effect of Zn Content on the Microstructure and Properties of Super-High Strength Al-Zn-Mg-Cu alloys. *Metall. Mater. Trans. A* **2013**, *44*, 3910–3920. [[CrossRef](#)]
22. Deiasi, R.; Adler, P.N. Calorimetric Studies in 7000 Series Aluminum Alloys: I. Matrix Precipitate Characterization of 7075. *Metall. Mater. Trans. A* **1977**, *8*, 1177–1183.
23. Liang, R.; Khan, A.S. A critical review of experimental results and constitutive models for BCC and FCC metals over a wide range of strain rates and temperatures. *Int. J. Plast.* **1999**, *15*, 963–980. [[CrossRef](#)]
24. Embury, J.D.; Nicholson, R.B. The nucleation of precipitates: The system Al-Zn-Mg. *Acta Metall.* **1965**, *13*, 403–416. [[CrossRef](#)]
25. Wert, J.A. Identification of precipitates in 7075 Al after high-temperature aging. *Scr. Mater.* **1981**, *15*, 445–447. [[CrossRef](#)]
26. Chang, Y.L.; Hung, F.Y.; Lui, T.S. Enhancing the tensile yield strength of A6082 aluminum alloy with rapid heat solutionizing. *Mater. Sci. Eng. A* **2017**, *702*, 438–445. [[CrossRef](#)]
27. Fujita, H.; Tabata, T. Discontinuous deformation in Al-Mg alloys under various conditions. *Acta Metall.* **1977**, *25*, 793–800. [[CrossRef](#)]
28. Misha, R.S.; Mahoney, M.W.; McFadden, S.X.; Mara, N.A.; Mukherjee, A.K. High strain rate superplasticity in a friction stir processed 7075 Al alloy. *Scr. Mater.* **2000**, *42*, 163–168. [[CrossRef](#)]

29. Chen, C.M.; Kovacevic, R. Finite element modeling of friction stir welding-thermal and thermomechanical analysis. *Int. J. Mach. Tools Manuf.* **2003**, *43*, 1319–1326. [[CrossRef](#)]
30. Worthington, P.J.; Brindley, B.J. Serrated yielding in substitutional alloys. *Philos. Mag.* **1969**, *19*, 1175–1178. [[CrossRef](#)]
31. Rodriguez, P. Serrated plastic flow. *Bull. Mat. Sci.* **1984**, *6*, 653–663. [[CrossRef](#)]
32. Li, X.M.; Starink, M.J. Identification and analysis of intermetallic phases in overaged Zr-containing and Cr-containing Al–Zn–Mg–Cu alloys. *J. Alloys Compd.* **2010**, *509*, 471–476. [[CrossRef](#)]
33. Pardoeny, T.; Brechet, Y. Influence of microstructure-driven strain localization on the ductile fracture of metallic alloys. *Philos. Mag.* **2004**, *84*, 268–297. [[CrossRef](#)]
34. Hecker, S.S. Formability of aluminum alloy sheets. *J. Eng. Mater. Technol.* **1975**, *97*, 66–73. [[CrossRef](#)]



© 2018 by the authors. Licensee MDPI, Basel, Switzerland. This article is an open access article distributed under the terms and conditions of the Creative Commons Attribution (CC BY) license (<http://creativecommons.org/licenses/by/4.0/>).